DEPARTAMENT D'ASTRONOMIA I METEOROLOGIA

UNIVERSITAT DE BARCELONA

Near-relativistic electron events. Monte Carlo simulations of solar injection and interplanetary transport

Memòria presentada per
Neus Àgueda Costafreda
per optar al grau de Doctora
per la Universitat de Barcelona.
Barcelona, 20 de febrer de 2008

5 Study of solar near-relativistic electron events. I

In this chapter, we apply the deconvolution procedure described in Chapter 4 to the study of NR electron events observed by the EPAM/LEFS60 telescope. The aim of the analysis is to provide insights into the conditions of the transport of solar NR electrons in the interplanetary medium and into the roles that flares and CME-driven shocks play in their injection. We first discuss the criteria adopted to select seven NR electron events. Then, we analyze the two events of the set that show a short (< 15 min) rise phase[1]. In chapter 6, we apply the same procedure to the other five electron events.

5.1 Selection criteria

With the goal of carrying out a precise study of the solar injection and the subsequent interplanetary transport of NR electrons, we consider seven NR electron events observed by the LEFS60 telescope between 1998 and 2004 that meet the following criteria:

- Quietness in the interplanetary medium (IMF and solar wind) from one hour prior to the onset of the event up to the end of the selected time period.
- Large-scale structure of the IMF close to the nominal Parker spiral.
- Significant enhancement of NR electron intensities (i.e. peak intensities at least one order of magnitude higher than the pre-event background).
- Negligible proton contamination in the electron energy channels of the LEFS60 telescope.
- Large pitch-angle cosine coverage of the LEFS60 telescope, μ-co $\geq 70\%$, and coverage of particles propagating antisunward along the field direction (section 4.2.1).

[1] See section 5.1.2

Table 5.1: Selected NR electron events

Event			Period	
Year	Date	DOY	(UT)	Name
1998	May 27	147	13:30–17:30	May98
2000	May 1	122	10:25–12:00	May00
2000	Jul 14	196	10:40–13:30	Jul00
2001	Apr 15	105	14:00–18:00	Apr01
2001	Dec 26	360	05:30–09:00	Dec01
2002	Oct 20	293	14:20–18:00	Oct02
2004	Sep 19	263	17:19–20:45	Sep04

It is more an exception than the rule that all these conditions are completely fulfilled in one specific event. Particle events with NR electron fluxes high enough to allow the derivation of meaningful values of the transport parameters are scarce. On the other hand, powerful events that generate high particle intensities frequently occur during periods of enhanced solar activity, when preceding events might have already populated the flux tubes connected with the observer and CMEs propagating in interplanetary space distort the nominal IMF topology. Table 5.1 lists the selected NR electron events; the first three columns give the year, date and day of the year (DOY) when the event occurred; the fourth column shows the time interval selected for the study of the event; the last column lists the short name assigned to each event.

In the following sections, we characterize these events by (1) the solar wind and IMF observations, (2) the intensity profiles observed at 1 AU, and (3) the correlations between NR electron observations and the electromagnetic emissions observed at the Sun.

5.1.1 Solar wind and IMF

Solar wind speed is a key parameter in the analysis of SEP events, since it determines two important quantities: the path length and the nominal footpoint of the field line connecting the observer to the Sun. The path length determines the transit time of the NR electrons propagating scatter-free along the IMF line from close to the Sun up to 1 AU. The nominal footpoint of the field line connecting the observer to the Sun can be used to estimate the angular distance between the site where NR electrons are presumably injected into the interplanetary medium and the location of the electromagnetic emissions observed at the Sun.

Table 5.2 lists the average properties of the solar wind and the IMF, as measured by *ACE*, for each one of the selected events. Although the IMF and solar wind data are local measurements taken at 1 AU, both the stability of the solar wind and IMF direction together with

Table 5.2: Solar wind and IMF properties

Event	Solar wind		IMF at 1 AU			
	$\langle u \rangle$	footpoint	$\langle \theta \rangle$	$\langle \phi \rangle$	polarity	
	(km s^{-1})	(°)	(°)	(°)	mode	%
1998 May 27	354± 4	W68	-4±22	153±38	−1	99
2000 May 1	437±19	W55	-8±25	141±21	−1	100
2000 Jul 14	593±12	W40	-14±37	321±37	+1	96
2001 Apr 15	502±10	W48	-19±27	164±70	−1	76
2001 Dec 26	374± 7	W64	28±20	177±31	−1	93
2002 Oct 20	642±21	W37	-6±22	130±16	−1	100
2004 Sep 19	376± 4	W64	-4±13	310±16	+1	100

the proximity of the IMF direction to the nominal Parker spiral direction assures that in the selected events the assumption of a Parker spiral for the IMF topology is reasonable. The first column in Table 5.2 lists the events. The following two columns give the mean value of the solar wind speed measured from one hour prior to the onset of the event up to the end of the period considered in Table 5.1 and the corresponding nominal footpoint, calculated using the solar wind speed. The next two columns give, respectively, the mean RTN latitude, $\langle \theta \rangle$, and the mean RTN longitude, $\langle \phi \rangle$[2]. The value of the modal polarity of the IMF (defined in section 4.2.2) and the prevailing period percentage are given in the last two columns.

As can be seen, the events show a stable solar wind speed ranging from 300 to 700 km s^{-1} with a mean standard deviation smaller than 3%. The magnetic field orientations have standard deviations of less than 40° in both latitude and longitude, and modal polarities prevail during ~90% of the periods under study. By contrast, the Apr01 event shows a rather large standard deviation in longitude (70°) and its modal polarity prevails only during 76% of the studied period.

5.1.2 Characteristics of the NR electron events

We analyze 72-s averages of the electron sectored intensities measured by the LEFS60 telescope in the energy range 62–312 keV. We do not include the lowest energy channel of the telescope, E'1 (45–62 keV), because of possible contribution from higher energy particles (see section 2.2).

We base the selection of the events on two key parameters: the strength of the event and the pitch-angle cosine coverage of the LEFS60 telescope during the event. We define the event strength, S, as the logarithm of the ratio between the spin-averaged peak intensity, I_P, and the

[2] θ is the magnetic RTN latitude in degrees with 0° in the B_R– B_T plane, and positive toward increasing B_N. ϕ is the RTN longitude in degrees with 0 at B_R and positive toward increasing B_T.

Table 5.3: Properties of the NR electron events

Event	Timing (E'4)		Strength, S			LEFS60	Spectral index
	t_0 (UT)	Rise (min)	E'4	E'3	E'2	μ-co	γ
1998 May 27	13:30	57	1.5	1.9	2.1	88%	3.3
2000 May 1	10:25	11	2.8	2.9	2.8	71%	2.4
2000 Jul 14	10:37	1561	1.4	1.6	1.5	85%	1.6
2001 Apr 15	14:02	142	2.0	2.0	1.8	87%	1.8
2001 Dec 26	05:27	84	2.9	3.0	3.2	76%	2.5
2002 Oct 20	14:22	5	1.6	2.1	1.8	84%	2.6
2004 Sep 19	17:19	85	2.2	2.4	2.4	88%	2.1

spin-averaged mean intensity of the pre-event background, I_b, in the same energy channel; thus $S = \log_{10}(I_P/I_b)$. We require $S > 1$ in E'2, E'3 and E'4 energy channels, in order to assure that the peak intensities are at least one order of magnitude higher than the pre-event background. We also require the mean pitch-angle cosine coverage to be high, μ-co $\geq 70\%$, during the event and that the telescope scan particles coming field aligned.

In order to characterize the electron events, we determine both the onset time and the rise period (defined as the time interval between the onset and the maximum intensity) of the spin-averaged time-intensity profile in the E'4 channel. We determine the onset of the event by means of the Poisson-CUSUM method (Huttunen-Heikinmaa et al. 2005). We also calculate an upper limit of the spectral index of the source by fitting a power law to the differential peak intensity of the sectors observed in each energy channel (Simnett 2005a). In the context of weak scattering and simultaneous release of accelerated particles at all energies, those particles traveling along the field line, without experiencing the scattering along the connecting IMF line, arrive first at the spacecraft. Thus, in principle, observed intensities do not reach maxima at the same time for different energy channels, because of their differences in propagation time. Nevertheless, if the interplanetary scattering is important, this method only provides an upper limit of the spectral index of the source. Since we do not know a priori what the conditions of the particle transport are, we take this value as an initial input parameter of the particle transport model and we aim to deduce a better estimation from the deconvolution of the event.

Table 5.3 gives, for each event, the inferred onset time and the rise period in the E'4 energy channel; the event strength, S, in the E'4, E'3, E'2 energy channels; the mean μ-co of the LEFS60 telescope for the selected period; and the estimated differential intensity spectral index. The events display a variety of rise periods: two events (May00 and Oct02) show a short rising phase (< 15 min), while the others show longer rise periods (up to one day). As a whole, the events show a median event strength of 2.2 orders of magnitude and a reasonably

good coverage (μ-co $\geq$ 70%) for their study. There is no correlation between the rise time and the μ-co, since we require the observation of antisunward field aligned particles. The mean differential intensity spectral index is of 2.3 ± 0.6.

In all cases, intensities observed by the LEFS60 telescope from one hour prior up to the onset of the event stay relatively quiet and isotropic (no significant differences among different sectors) . Therefore, we might consider that the flux tubes were not populated with electrons from previous solar events.

We use 72-s spin-averaged 53–315 keV deflected electron intensities observed by the pure electron channels of the EPAM/DE telescope for comparison. We require similar trends (small differences may be caused by anisotropy) that assure that contamination in the electron energy channels of the LEFS60 telescope is negligible. In addition, we take into account the correlation between the NR electron event and the proton event (when observed). To characterize the proton event, we use 8-min spin-averaged 1.06–4.80 MeV proton intensities observed by the EPAM/LEMS120 telescope and 1.33–4.75 MeV proton intensities observed by ERNE. In particular, we use LEMS120 measurements in the P'7 (1.06–1.90 MeV) and P'8 (1.90–4.80 MeV) energy channels to compare with ERNE 1.33–1.90 MeV and 1.90–4.75 MeV energy channels.

5.1.3 Associated electromagnetic emissions

We use observations reported by *SGD* to identify both the Hα flares associated with each NR electron event and the characteristics of the soft X-ray event. In addition, we include hard X-ray observations from *Yohkoh* and *RHESSI*, whenever available (S. Pohjolainen; 2008, private communication). We obtain the characteristics of the CMEs (speed, width, time) observed in association with the NR electron event from the *SOHO*/LASCO CME catalog[3]. Associations are made primarily on the basis of location and timing information.

Table 5.4 summarizes the properties of the electromagnetic emissions observed in association with the selected NR electron events. In both the upper and lower part of the table, the first column gives the date of the event. In the upper part of the table, the three following columns give the characteristics of the soft X-ray flare (start time, rise period and class). The next four columns give the characteristics of the Hα flare (start time, rise period, importance and location). The last column gives the absolute value of the difference between the heliolongitude of the Hα flare and the nominal footpoint of the Parker spiral magnetic field (listed in Table 5.2). In the lower part of the table, the second and third columns give the characteristics of the hard X-ray emission (start time and duration); the last four columns give

[3] `http://cdaw.gsfc.nasa.gov/CME_list/`

Table 5.4: Electromagnetic emissions associated with the electron events

Event	Solar Flare							Δ
	Soft X-rays			Hα				
	Start (UT)	Rise (min)	X-ray class	Start (UT)	Rise (min)	Imp. opt	Position	(°)
1998 May 27	13:10	25	C7.5	13:16	12	SF	N18W60	7
				12:40	32	SF	S12W80	13
2000 May 1	10:16	11	M1.1	10:09	7	SN	–	1
2000 Jul 14	10:03	21	X5.7	10:12	9	3B	N22W07	33
2001 Apr 15	13:19	31	X14.4	13:36	13	2B	S20W85	37
2001 Dec 26	04:32	68	M7.1	04:32	42	1B	N08W54	10
2002 Oct 20	14:10	3	C6.6	14:11	4	SF	S13W63	26
	14:21	7	M1.8	14:22	2	1B	S19W23	14
2004 Sep 19	16:46	26	M1.9	16:11	No flare patrol		–	6

Event	Solar Flare		CME				Ref.
	Hard X-rays						
	Start (UT)	Duration (min)	First Ob. (UT)	PA (°)	Speed (km s^{-1})	Width (°)	
1998 May 27	07:48	–	13:45	175	878	268	(1),(2)
2000 May 1	10:20	3	10:54	323	1360	54	(3),(4)
2000 Jul 14	10:24	15	10:54	Halo	1674	360	(4)
2001 Apr 15	13:44	11	14:06	245	1199	167	(4)
2001 Dec 26	–	–	05:30	281	1446	>212	(5)
2002 Oct 20	14:22	7	14:30	247	1011	20	(6)
2004 Sep 19	16:48	15	22:18	262	-	99	(5)

(1) Torsti et al. (2002); (2) Klein et al. (2005); (3) Kahler et al. (2001); (4) Cane et al. (2002); (5) Cane et al. (2006); (6) Pick et al. (2006); and *SGD*.

the parameters of the CME as reported in the *SOHO*/LASCO CME catalog: time of the first appearance in the C2 coronograph, position angle (PA, measured counterclockwise from the conventional solar north), plane-of-sky speed[4] of the leading-edge and angular width. The last column quotes previous works that have made the same flare/CME association.

Each NR electron event is clearly associated with an intense soft X-ray flare of variable duration. Five events (May00, Jul00, Apr01, Dec01 and Sep04) are associated with a single active region. Two events (May98 and Oct02), however, have been associated with two western active regions (see further comments in sections 6.3 and 5.3, respectively). Five events (May98, Jul00, Apr01, Dec01 and Oct02) are clearly associated with an Hα flare reported in *SGD*. All the events have $\Delta < 40^\circ$ and therefore can be considered magnetically well connected to the flare site (Wibberenz & Cane 2006).

As can be seen in Table 5.4 (bottom), each NR electron event is associated with a CME observed by LASCO, with a leading edge that was distinct enough to be mapped. In all cases the CME was first observed after the start of the soft X-ray event, typically by ~10 to 60 minutes. In one case (Sep04) the CME was first observed in the C3 coronograph images about five hours after the start of the soft X-ray event, when it was already above 30 $R_\odot$. It was not reported when it was closer to the Sun because the C2 coronograph was unavailable at that time. All of the CMEs have PA > 180° and high plane-of-sky velocities ($\geq$ 850 km s^{-1}). Five of them (May98, Jul00, Apr01, Dec01 and Sep04) have angular widths greater than ~100°; whereas two events (May00 and Oct02) were associated with two narrow (< 60°) CMEs.

All the selected events are clearly preceded by type III fast-drift radio bursts observed by the *Wind*/WAVES experiment. In most cases, these bursts are the dominant feature of the dynamic spectrum of the day. Using these spectral plots, the start and end times of the bursts associated with each electron event are estimated at 14 MHz, to the nearest 5 minutes (Table 5.5). A more accurate time could be obtained by examining individual frequency profiles. The start and end times of the bursts associated with the electron events prior to year 2002 have been checked with the values reported by Cane et al. (2002).

The last three columns of Table 5.5 list the type II radio bursts reported in association with the electron events, giving the duration of the type II emission, the frequency range and some comments on the observed radio phenomena[5]. Only for the 2001 December 26 event is a strong type II burst identified, clearly extending below 10 MHz and exhibiting harmonical bands. The rest of the reported type II-like emissions show a diversity of radio phenomena but are weak, broadband and sporadic. Cane & Erickson (2005) pointed out that most metric

[4]We assume that, within the accuracy of the measurements, the CMEs have a constant velocity close to the Sun, as suggested by Wen et al. (2007).

[5]Extracted from `http://www-lep.gsfc.nasa.gov/waves/waves.html`

Table 5.5: Radio emission associated with the electron events

Date	Type III	Type II		
	Time (UT)	Time (UT)	Freq Range (kHz)	Comments
1998 May 27	13:15–13:30	13:30–14:20	4000–1000	Weak,intermittent
2000 May 1	10:20–10:25	—	—	—
2000 Jul 14	10:20–10:50	10:30–14:30	14000–80	Extremely broadband, mostly harmonic
2001 Apr 15	13:45–14:15	14:05–13:00^{+}	14000–40	Occasional F-H visible
2001 Dec 26	05:15–05:20	05:20–05:00^{+}	14000–150	Strong F-H
2002 Oct 20	14:10–14:15 14:25–14:40	—	—	—
2004 Sep 19	16:55–17:30	17:15–18:15	14000–2500	Very sporadic

(+ : emission extends to the next day)

type II bursts fade out before reaching 20 MHz[6].

In the following sections, we first analyze each NR electron event from the point of view of the observations (the electromagnetic proxy emissions and the characteristics of in-situ SEPs observed at 1 AU). Then, we present the results of the application of the deconvolution algorithm. We begin the analysis with the two electron events that show a short rise phase in the E'4 energy channel, May00 and Oct02. In chapter 6, we continue with the analysis of the five other events in order of increasing Δ, that is, Sep04, Dec01, May98, Jul00 and Apr01.

5.2 The 2000 May 1 event

5.2.1 Electromagnetic emissions

The solar activity associated with the origin of the May00 event has been widely studied. An impulsive M1.1 X-ray flare with onset at 10:16 UT and maximum at 10:27 UT was the largest solar event observed on that day (Cane et al. 2002). Kahler et al. (2001) identified a compact brightening in NOAA active region AR 8971 approximately at N20W54 with maximum intensity in the 10:24 UT image associated with the M1.1 flare. No accompanying Hα flare was reported. The beginning of the hard X-ray emission was observed at 10:20 UT by *Yohkoh*/HXT and it lasted ~3 min.

[6]These authors stressed the importance of including ground-based data, with a higher frequency coverage range than WAVES, in any study in order to help to discern WAVES blobs and bands from actual type II bursts.

Kahler et al. (2001) also associated a fast-moving (1360 km s^{-1}) narrow ($\sim 20°$) CME with the origin of the SEP event. The CME structure was first seen in LASCO images above 2 $R_\odot$ at 10:54 UT (Kahler et al. 2001). Kallenrode (2003) pointed out that narrow CMEs like this one do not necessarily correspond to the classical picture of CMEs. Rather, they look like jets or plasmoids that are ejected upward from magnetic reconnection sites over active regions, which in turn might produce shock-excited radio bursts. Kallenrode (2003) suggested that the shocks associated with these narrow jet-like CMEs do not necessarily accelerate particles.

Pick et al. (2003) reported the beginning of a type III radio emission around 10:19 UT on 2000 May 1. These authors observed a series of type III metric radio sources at about the same position angle as the C2 LASCO feature, with a velocity of about 1470 km s^{-1}, that extrapolated well into the height-time curve of the coronograph narrow feature. These observations were consistent with a release of energetic electrons from the corona, in the region where magnetic reconnection ejected upward the moving radio and C2 LASCO feature. Maia & Pick (2004) concluded that the May00 event was not accompanied by a typical CME, but associated with an outward moving radio source.

Pick et al. (2006) identified the source of this SEP event from radio and optical imaging in addition to energetic ion and electron data, together with calculated coronal fields obtained from extrapolating photospheric magnetograms using the potential field source surface model (Schatten et al. 1969). Pick et al. (2006) concluded that, although the narrow jet-like CME was directed $\sim 50°$ out of the ecliptic plane, the injected particles could promptly reach 1 AU by following the open field lines that connected the source region to the ecliptic plane. Thus, the accelerated particles were not constrained to follow the same trajectory as the bulk of the CME.

5.2.2 In-situ energetic particles

Figure 5.1 shows the spin-averaged 62–312 keV electron intensities observed by the EPAM-/LEFS60 telescope. The first NR electrons were detected above the pre-event background around 10:25 UT in the E'4 channel (175–312 keV). The maximum spin-averaged intensity was observed at 10:36 UT in the E'4 channel, at 10:39 UT in the E'3 channel (102–175 keV) and at 10:46 UT in the E'2 channel (62–102 keV). For comparison, the first panel in Figure 5.1 shows the electron intensities observed by the DE detector (thin line) with the same scale factors as used for the intensities measured by LEFS60. The similarity of the trends suggests that there is negligible proton contamination in the LEFS60 NR electron profiles.

The top panel in Figure 5.1 also includes the proton intensities observed by the LEMS120

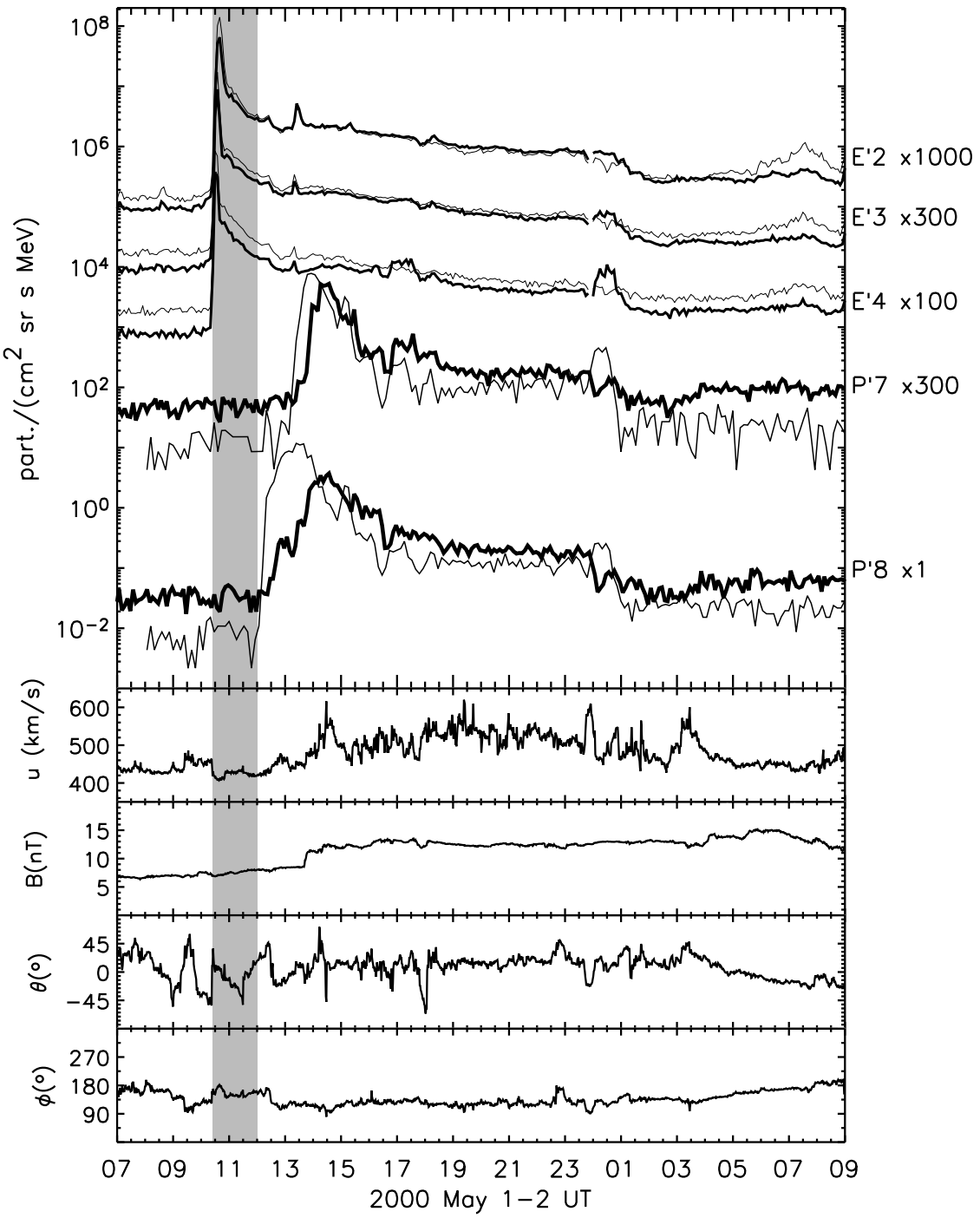

Figure 5.1: Particle event on 2000 May 1. From top to bottom: Electron and proton spin-averaged intensities observed by the LEFS60 and the LEMS120 telescopes on board ACE. Deflected electron intensities and proton intensities observed by ERNE telescope are shown with a thinner line (see text for details). Solar wind velocity observed by ACE/SWEPAM. Magnetic field magnitude, latitude (θ) and longitude (ϕ) measured by the ACE/MAG experiment in the RTN coordinate system. The gray area indicates the period of study of the electron event.

telescope and by the ERNE telescope (thin line) between 1 and 5 MeV approximately. The LEMS120 telescope is oriented 120° with respect to the *ACE* spin axis, thus its look direction is opposite to the Sun. In contrast, ERNE measures particle intensities coming from the Sun within a limited field-of-view aligned with the nominal Parker field direction. Although these two instruments are not cross-calibrated, we are able to compare their measurements since both measured the same intensity values late in the event (~20:00 UT), when these profiles became almost flat (the same scale factor is applied to the ERNE profiles). As can be seen in Figure 5.1, at the beginning of the event the proton intensity profiles at the two instruments were very different, thus the event was highly anisotropic.

We will study the electron event observed by EPAM/LEFS60 from 10:25 UT to 12:00 UT (gray area in Figure 5.1). The onset of the 1.90–4.75 MeV proton event took place around 12:05 UT; thus, we restrict the study to the period when the associated proton event had not started yet.

This SEP event displays all basic features to be classified as impulsive: high (>1) Fe/O and ^{3}He/^{4}He ratios (Mason et al. 2002), low (~10) H/He ratios (Kahler et al. 2001) and an extremely anisotropic onset (Ho et al. 2003). The prompt phase of the NR electron event is well defined, however, as can be seen in Figure 5.1, the intensities of both electrons and protons remained at high levels for an extended period (~15 h) after the flare, probably indicating a gradual injection component from the CME-driven shock.

The four lower panels in Figure 5.1 show the solar wind velocity, the IMF magnitude and the IMF direction (θ is the latitude and ϕ is the longitude, in the RTN spacecraft coordinate system). SWEPAM data indicate that at the onset of the event, *ACE* was embedded in a solar wind stream with a mean velocity of 437 km s^{-1}. Both the solar wind velocity and the IMF direction were relatively stable through the rising phase of the electron event. Therefore, the Parker IMF model and the assumptions adopted in the model for particle propagation are reasonable approximations. The nominal footpoint of the field line connecting *ACE* to the Sun was at a western longitude of 55°, as estimated from the observed solar wind speed, being close to the longitude of the flare site (W54).

Since adiabatic deceleration is not important for NR electrons in the impulsive phase of the event, the spectral index of the electron source can be estimated by fitting a power-law to the maximum sectored intensity observed in each energy channel within the period of study of the event, following the procedure applied by Simnett (2005a). The spectral index of the derived differential intensity spectrum is estimated by $\gamma = 2.4$. Therefore, we assume $\gamma_s = 2.9$ as a first approximation of the spectral index of the source (see section 3.6).

5.2.3 Deconvolution of the NR electron event

Figure 5.2 shows the 72-s *ACE*/MAG magnetic field measurements, the range of μ-values scanned by the LEFS60 telescope and the μ-co of the telescope for the period studied. The first three panels show the magnetic field vector in spherical coordinates (magnitude, polar angle, θ_B, and clock-angle, ϕ_B) in the spacecraft coordinate system. The first panel also includes the IMF polarity (thin line) calculated by means of Equation (4.10). The fourth panel shows the range of μ-values scanned by the telescope (gray area) and the mean pitch-angle cosine scanned by each sector as a function of time. The bottom panel shows the μ-co of the telescope. The vertical dotted lines indicate the time period selected to deconvolve the NR electron event.

As can be seen in Figure 5.2, the IMF polarity remains negative during this period; this means that electrons coming from the Sun along the field lines have $\mu = -1$. The μ-co of the telescope varies between 50% and 80%, with a mean coverage of μ-co $\sim$71%. The combination of μ-co $\geq$ 70% and the observation of particles propagating antisunward along the field direction (see gray area in panel four of Figure 5.2) ensures that there is enough information in the sectored data to deconvolve the NR electron event.

Note, however, that right at the beginning of the period there is a decrease of the θ_B value which results in a loss of coverage of the telescope[7] (down to 50%) for a period of $\sim$20 min. Therefore, the LEFS60 telescope covers the forward hemisphere ($\mu \leq 0$) of the PADs and part of the backward hemisphere ($0 < \mu \leq 0.5$) during most of the selected time period. However, from 10:30 to 10:50 UT the backward hemisphere is only slightly scanned by the telescope.

In order to apply the deconvolution technique described in section 4.1, we vary the value of the radial mean free path λ_r from 0.1 to 1.6 AU with step intervals of 0.1 AU and we consider three scattering cases: isotropic scattering and two models of μ-dependent scattering, with $\epsilon = 0.10$ and $\epsilon = 0.01$. The calculation of the goodness-of-fit is restricted to the time interval from 10:25 to 12:00 UT and, therefore, we force the particle injections producing an onset before 10:25 UT to be zero. Each energy channel is separately fitted and the goodness-of-fit estimator of the whole fit is obtained by adding the values obtained for each energy channel, $\zeta = \sum_l \zeta_l$. Therefore, we assume that the value of λ_r that minimizes ζ is within 0.1 and 1.6 AU[8].

Figure 5.3 illustrates the dependence of the injection profile on the radial mean free path. The five top panels show examples of the 102–175 keV electron injection profiles derived for

[7] The loss of coverage was produced by the fact that the magnetic field vector was getting closer to the spin axis as θ_B decreased and therefore, all sectors were practically scanning the same μ range

[8] In the case that we had found that the lowest ζ corresponds to one of the two boundaries of the interval, it would have been necessary to expand the range in λ_r in order to ensure a local minimum in $\zeta(\lambda_r)$.

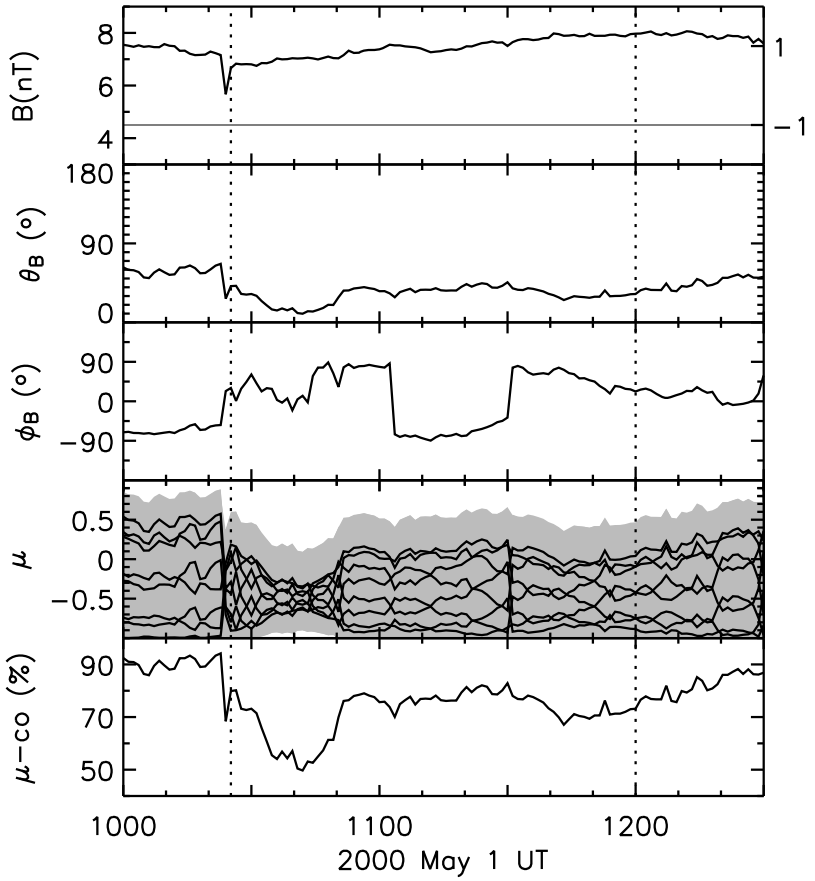

Figure 5.2: Three upper panels: Magnetic field magnitude and polarity (thin line), polar angle (θ_B) and clock-angle (ϕ_B) measured by the MAG experiment in the spacecraft coordinate system during 2000 May 1. Fourth panel: range of pitch-angle cosine scanned by the LEFS60 telescope (gray area) and pitch-angle cosine of each sector. Bottom panel: μ-co of the LEFS60 telescope.

the case of isotropic scattering, for different values of λ_r (the other cases and energies show similar behaviors). The lowest panel shows how the goodness-of-fit estimator changes as a function of λ_r. For a small λ_r, the deconvolution technique yields an impulsive injection and high ζ values. As λ_r increases, the injection profile becomes wider and the procedure gives lower ζ values. A very large λ_r increases ζ again because the prolonged injection produces high anisotropies that cannot adequately fit the intensities registered by the sectors not aligned with the IMF direction.

The deconvolution algorithm allows us to objectively identify (within the constraints of the model) the best possible fit for all eight sectors. The lowest values of ζ obtained for each scattering case are listed in Table 5.6. Figure 5.4 shows the fit for the case with the lowest ζ. Each of panels 1 through 8 displays the observed and modeled intensities for the three energy channels (E'2, E'3, E'4) in each sector (top) and the evolution of the pitch-

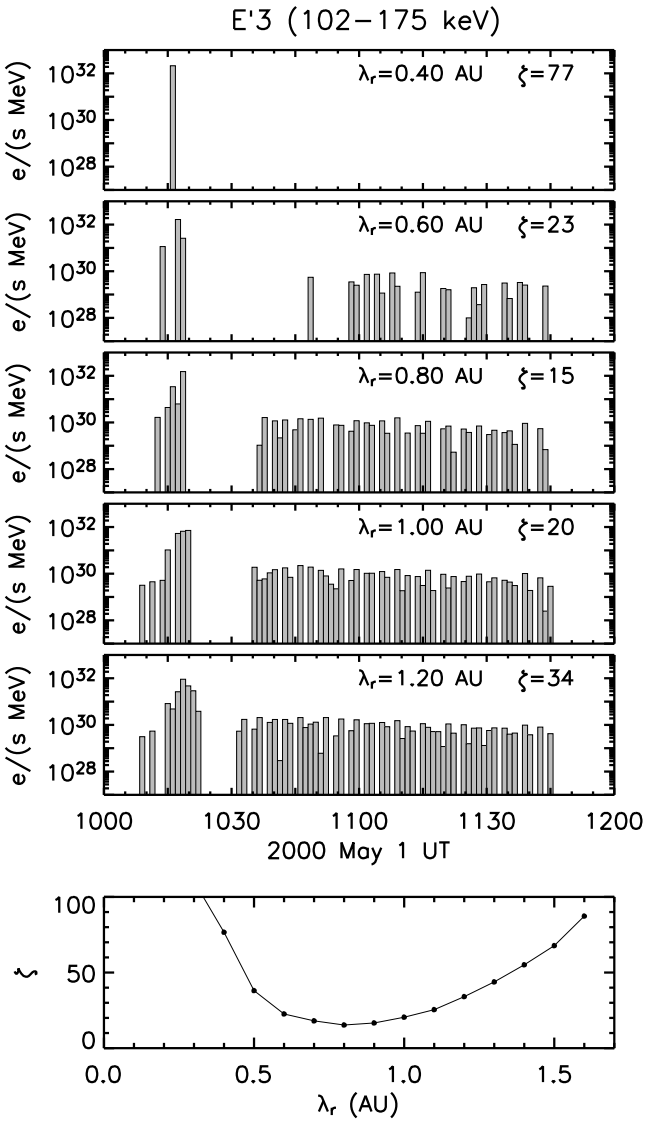

Figure 5.3: Five top panels: 102-175 keV NR electron injection profiles as a function of the radial mean free path for the case with isotropic scattering. The bottom panel displays the goodness-of-fit estimator ζ corresponding to the E'3 channel as a function of λ_r.

angle cosine μ of the midpoint clock-angle zenith direction of the sector as a function of time (bottom). The bottom panel also shows the pitch-angle cosine range scanned by each sector as a function of time (gray area). We emphasize that for each energy channel, all eight profiles are optimized simultaneously for the whole time period. The last panel in Figure 5.4 displays the omnidirectional intensities (top) and the evolution of the mean pitch-angle cosine (bottom) as deduced from the modelization of the three energy channels. The gray area displays the range of pitch-angle cosines scanned by the LEFS60 telescope as a function of time.

The best fit corresponds to $\lambda_r = 0.9$ AU and μ-dependent scattering with $\epsilon = 0.01$. The

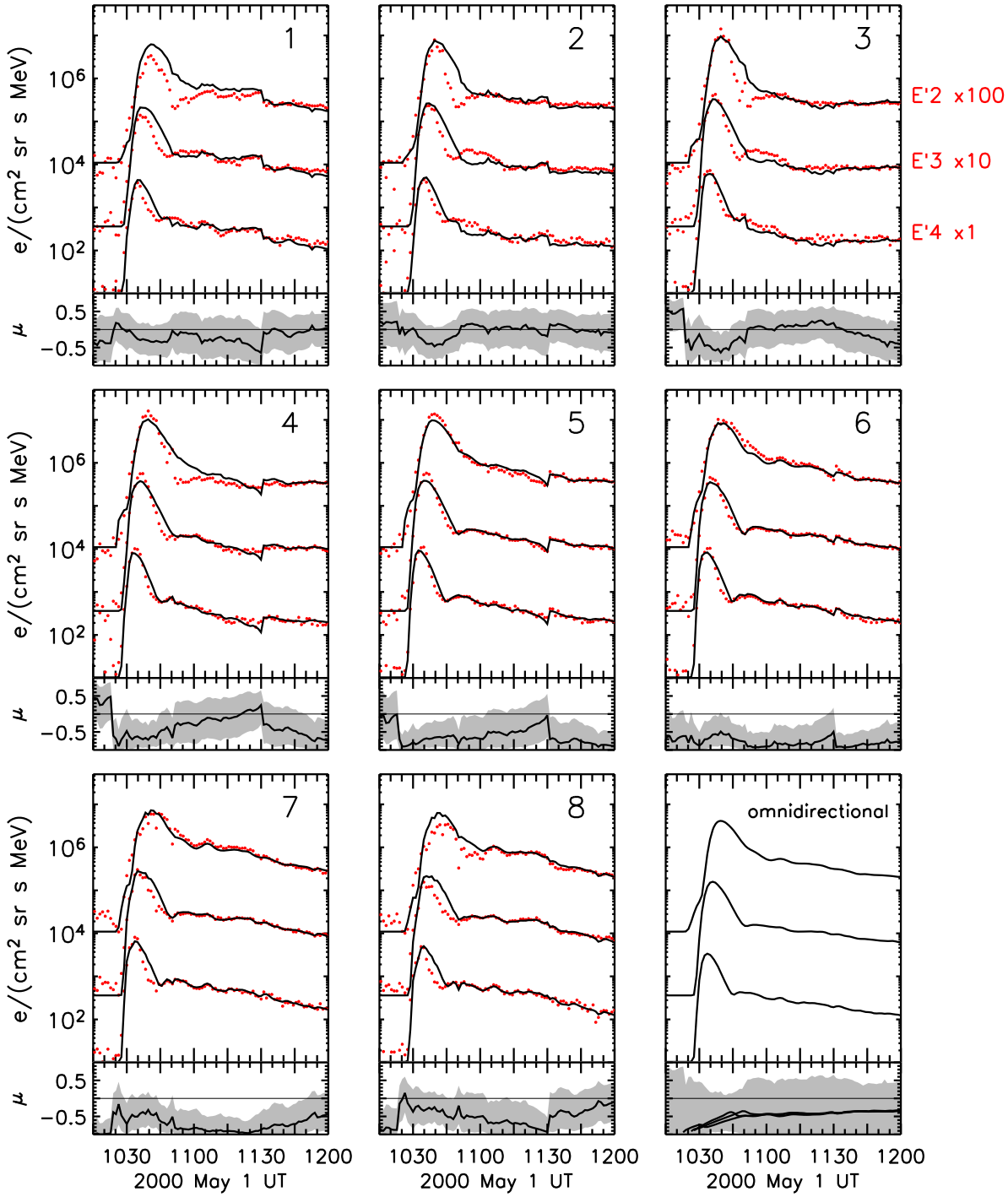

Figure 5.4: NR electron event on 2000 May 1 as observed by the LEFS60 telescope on board ACE/EPAM. Electron sectored intensities E'4, E'3 (×10), and E'2 (×100). Sectors are labeled from 1 to 8. Black curves show the modeled sectored intensities and red dots show the observational data. Low panels show the pitch-angle cosine of the midpoint clock-angle zenith direction of the sector (black line) and the scanned pitch-angle cosine range (gray area) as a function of time. The last panel shows the omnidirectional intensities and the mean pitch-angle cosine as a function of time as deduced from the simulation. The gray area shows the pitch-angle cosine range scanned by the LEFS60 telescope.

Table 5.6: Results of the fit

Scattering case	ζ {E'2, E'3, E'4}	λ_r (AU)
Isotropic scattering	{28, 15, 17} = 60	0.8
μ-dep with $\epsilon = 0.10$	{23, 14, 13} = 50	0.9
μ-dep with $\epsilon = 0.01$	{25, 14, 10} = 49	0.9

fit succeeds in reproducing most of the intensity profiles during ~90 min. However, discrepancies between the simulated and observed sectored intensities appear in the ~12 min following the intensity peaks. These differences are larger in the low energy channels and in the sectors not aligned with the instantaneous IMF (sectors 1, 2 and 8). There are at least two explanations for these discrepancies: (1) the model is overestimating the scattering processes at work (i.e. the simulated particles do not propagate along the IMF flux tube as fast as the actual electrons do). Thus, it is possible that more involved models with a wider resonance gap near $\mu = 0$ or with a spatially varying ϵ, for example, might perform better. And (2), the detector response model is too simple; it only takes into account the angular features but not the energy response of the detector.

The values of the solar electron injection derived from the best fit are shown in the three top panels of Figure 5.5. For convenience of comparison with the observed solar electromagnetic emissions, electron injection times are shifted by 8 min to account for the light travel time. The injection profiles clearly show two components: one prompt component starting around 10:15 UT for E'2 and after 10:20 UT for E'3 and E'4 and lasting ~5 min, followed by a second weaker time-extended component starting at 10:35 UT and lasting for about ~80 min. The total number of injected NR electrons in the whole measurement range is $(3.6\pm0.5)\times10^{33}$ as determined by the normalization of fitting. A large fraction (~75 %) of the injection corresponds to the prompt injection component. At low energies (channel E'2) the prompt injection component seems to consist of two parts, separated by a few minutes. The second part (after 10:20 UT) is much larger than the first one, 98% of the whole prompt component. This first small component might reflect the fact that the model does not take into account the secondary responses of the instrument to electrons of higher energy, as clearly shown in the first enhancement of the E'2 time-intensity profile of Figure 5.4.

Haggerty & Roelof (2003) determined the secondary responses for the EPAM deflected electron channels and found that for hard spectra ($\gamma < 3$) DE2 and DE3 channels had strong responses to electrons of $\gtrsim$ 300 keV and $\gtrsim$ 250 keV, respectively, as well as to those electrons with the nominal energies of each channel (close to those of channels E'2 and E'3 of EPAM/LEFS60). The intensity profile in the rising phase of the event in E'2 is different from the other two higher energy channels (see Figure 5.4) and is typical of secondary responses

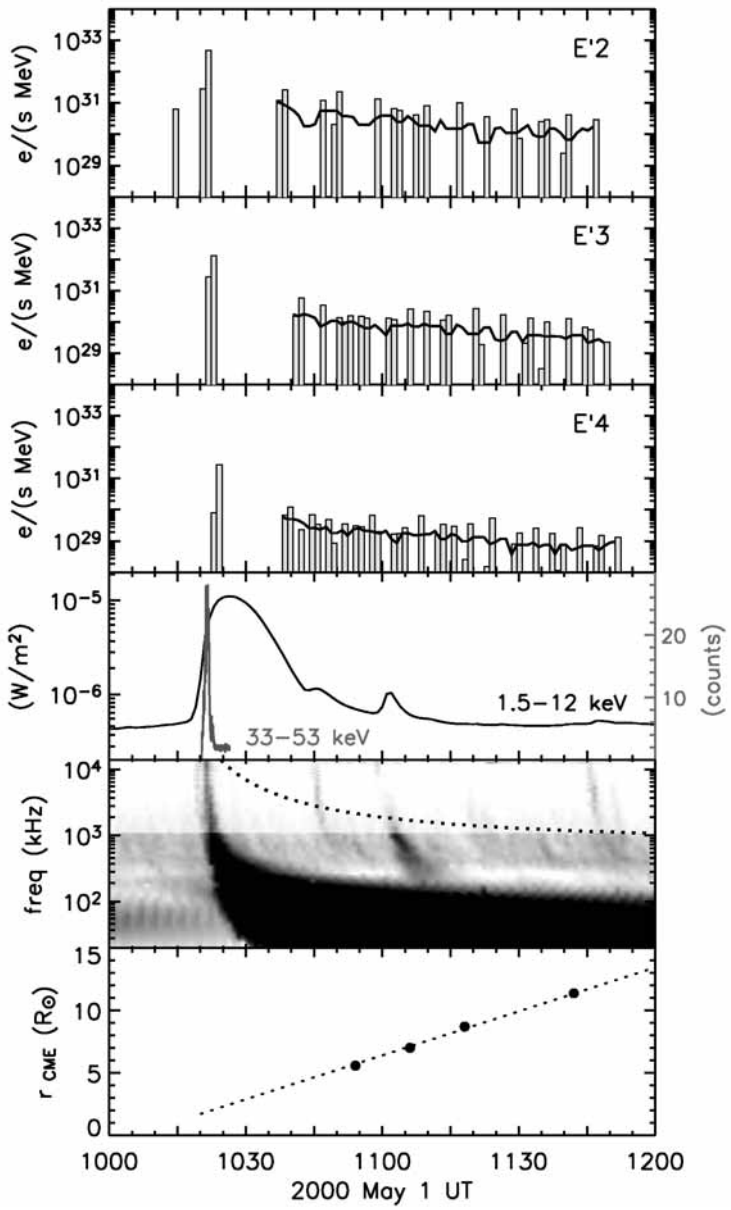

Figure 5.5: From top to bottom: NR electron injection profiles derived for the three modeled energy channels (injection times are shifted by 8 min to account for the light travel time). Soft (black line; left axis) and hard (gray line; right axis) X-ray flux profiles. Radio flux observed by Wind/WAVES. Dotted line shows the local electron plasma frequency at the height of the CME leading edge (Mann et al. 1999). Height-time plot of the CME leading edge from the SOHO/LASCO Catalog.

due to higher-energy electrons arriving at 1 AU faster than the electrons corresponding to the nominal energy window of E'2. Therefore, we assume that the actual prompt component injection is just the second part of this profile, starting after 10:20 UT in the E'2 energy channel.

Thus, we find that, in the studied energy range (62–312 keV), the prompt injection extents between 10:20 UT and 10:25 UT; it lasts ∼2.5 min in the three studied energy channels but the onset appears delayed the higher the energy. We can not state that the inverse energy injection onset has physical implications because we suspect that it could also be related to the fact that we are fitting the three energy channels separately.

The second injection component is patchy. This is probably due to the fact that the pitch-angle scattering case does not adequately describe the actual scattering processes at work and it tries to cope with the differences by temporally switching on and off the injection. Nevertheless, it is clear that the injection profile consists of two components. This is why, in the three top panels of Figure 5.5, we plot smoothed curves for the second injection component, calculated using a 6-point moving average. It is worth noting that by convoluting the modeled Green's functions by the smoothed injection profile, the obtained sectored intensities barely differ from the ones obtained for the patchy injection profile ($\zeta \simeq 49$).

By integrating the injection function over time for each energy channel, we can construct the time-integrated spectrum which corresponds to a piecewise normalized power-law spectrum with the assumed spectral index of $\gamma_s = 2.9$ in each energy channel. As the total number of electrons in the E'2 channel is a bit lower than what the assumed spectral index would demand, the spectrum can be best fit by a single power-law index if we take $\gamma_s = 2.7$. We find good agreement between the spectral index deduced from the time-integrated spectrum and the one estimated from the observations.

The three lower panels of Figure 5.5 compare the timing of the electron injection with the electromagnetic emissions observed at 1 AU. These plots show, from top to bottom, the soft (1.5–12 keV) and hard (33–53 keV) X-ray flux observed by *GOES*/XRS and *Yohkoh*/HXT, the radio flux observed by *Wind*/WAVES and the CME height-time plot obtained from the *SOHO*/LASCO Catalog. Neglecting the first part of the prompt electron injection in E'2 at 10:15 UT (probably related to secondary responses of this energy channel), the start of the prompt electron injection in E'2 coincides with the beginning of the hard X-ray emission and the start of the soft X-ray flare. Moreover, the timing of the type III burst is consistent with the start of the prompt injection in E'2. Comparing the times of the maximum injection to the electromagnetic emissions, we see that the time of maximum injection at the highest energies coincides with the maximum intensity of the soft X-ray emission.

The timing of the delayed injection component is a bit more uncertain since its onset is

still masked by the tail of the prompt component. It seems to start earlier than the second type III burst in Figure 5.5, which coincides with a small peak in the soft X-ray intensity around 10:46 UT. However, as the region near the minimum of the goodness-of-fit estimator $\zeta(\lambda_r)$ providing acceptable fits is rather extended, the actual value of the mean free path may be a bit smaller than the best-fit value. In this case, the delayed injection starts later than in the best-fit case and may coincide with the second type III burst. Interestingly, the third type III burst, starting right after 11:00 UT (and also related to a soft X-ray peak), is consistent with being originated from a source at a height of the CME leading edge if the density model of Mann et al. (1999)[9] is used (dotted curve in the fifth panel of Figure 5.5). Some faint fast-drifting radio bursts near 11:20 UT and 11:35 UT seem to originate from the CME leading edge as well. Maia & Pick (2004) already pointed out that the position of these successive type III-like radio sources extrapolate well into the height-time curve of the CME. This supports a scenario where the source of the delayed injection is at least partly provided by the CME-driven shock.

5.3 The 2002 October 20 event

5.3.1 Electromagnetic emissions

Observations indicate that there were three X-ray flares that could be related to the NR electron event observed on 2002 October 20. There was an impulsive C5.9 X-ray flare (onset at 13:51 UT and maximum at 14:02 UT) associated with an Hα flare at N21E50 (NOAA active region AR 10162). Shortly afterwards, a second C6.6 X-ray flare (onset at 14:10 UT and maximum 14:13 UT) was observed in association with an Hα flare located at S13W63 (AR 10154). The third and largest solar X-ray event (M1.8) was observed in association with an Hα flare located at S19W23 (onset at 14:21 UT and maximum at 14:28 UT). Hard X-ray emission at 25–50 keV started at 14:22 UT and lasted ~7 min. A fast-moving (1011 km s^{-1}) narrow (~20°) CME was firstly seen by LASCO above 2 $R_\odot$ at 14:30 UT (more details in

[9]The solar and interplanetary radio radiation is generated by plasma emission. The radio waves are emitted near the local electron plasma frequency $f = \sqrt{e^2 n/\pi m}$ (e and m, electron charge and mass; n, electron density) or its harmonics. Mann et al. (1999) derived a heliospheric density model by evaluating the spherical solutions of magnetohydrostatic equations supplemented by an isothermal equation of state and the gravitational force of the Sun. Then, from the radial density behavior, they obtained that the electron plasma frequency varies according to

$$f(r) = f_s \cdot \exp\left[\frac{A}{2R_\odot}\left(\frac{R_\odot}{r} - 1\right)\right] \tag{5.1}$$

where $N_s = 5.14 \times 10^9$ cm^{-3} and $A/R_\odot = 13.83$, if a temperature of 1×10^6 K in the range 1.02–3.00 $R_\odot$, and $f_s = 644$ MHz is assumed. A plasma frequency of 6.4 MHz is calculated at $r = 3$ $R_\odot$.

Table 5.4).

Figure 5.6 shows the radio emission observed on 2002 October 20 by the Nançay Decametric Array (20–70 MHz) and *Wind*/WAVES (0.02–14 MHz). Klein & Posner (2005) reported two type III radio bursts starting around 14:10 UT and 14:25 UT at 14 MHz, and lasting 5 and 15 min, respectively. The source of the first type III burst at 164 MHz projected onto the angular extent of the narrow CME observed by LASCO (Klein & Posner 2005). The emission of the second type III group was very weak. Klein & Posner (2005) reported extended faint loops seen in EIT images connecting the two western active regions. Since the nominal Earth-Sun connecting magnetic field line was rooted in between the locations of the two EIT brightenings, these authors proposed a release of particles from the two western flares. The association of both flaring active regions with metric-to-kilometric type III bursts demonstrated their connection to open interplanetary magnetic field lines. Klein & Posner (2005) also reported a type II burst in the 20–70 MHz range between 14:32 UT and 14:39 UT (see Figure 5.6).

Pick et al. (2006) studied the solar origin of the Oct02 SEP event from the analysis of in situ energetic ion and electron data, radio and optical images, together with calculated coronal fields obtained from extrapolating photospheric magnetograms. They concluded that there were open field lines that connected the narrow jet-like CME to the Earth and that therefore, injected particles could promptly reach a near-Earth spacecraft connected to the source region.

5.3.2 In-situ energetic particles

Figure 5.7 shows the spin-averaged 62–312 keV electron intensities observed by the EPAM-/LEFS60 telescope. The first NR electrons were detected above the pre-event background around 14:22 UT in the E'4 channel. The maximum spin-averaged intensity was observed at 14:27 UT in the E'4 channel, at 14:29 UT in the E'3 channel and at 14:33 UT in the E'2 channel. We will study this event for the period from 14:20 to 18:00 UT (gray area in Figure 5.7). For comparison, the top panel in Figure 5.7 shows the DE30 electron intensities (thin line). The similar trends suggest that there is negligible ion contamination in the LEFS60 NR electron profiles.

For completion, top panel in Figure 5.7 also includes the 8-min spin-averaged proton intensities observed by the LEMS120 telescope and by the ERNE telescope (thin line) between 1 and 5 MeV approximately[10]. As can be seen in Figure 5.7, no proton event was observed

[10] In Figure 5.7, the ERNE low energy channel (1.33–1.90 MeV) is multiplied by a factor of 0.5, whereas the high energy channel (1.90–4.75 MeV) is multiplied by 0.1.

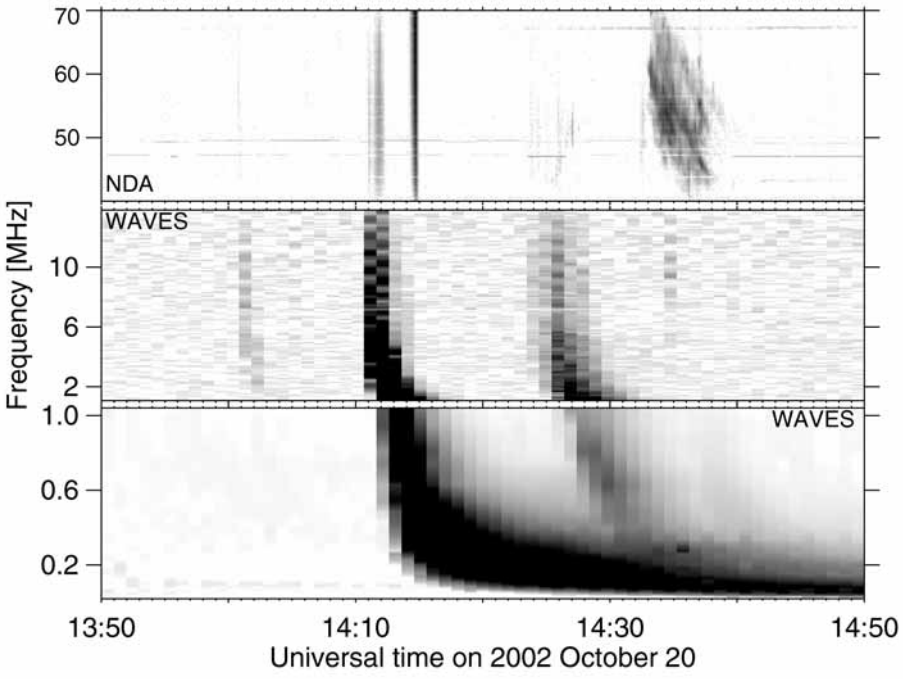

Figure 5.6: Oct02 event: Radio emission observed by the Nançay Decametric Array (NDA) and the Wind/WAVES experiment on 2002 October 20 (from Klein & Posner 2005); the vertical bar in the NDA spectrum near 14:15 UT, shortly after the first type III burst, is a calibration signal.

during the selected period of time. However, Pick et al. (2006) reported a small ^{3}He-rich enhancement at energies 0.2–10 MeV nucl^{-1} and a Fe/O ratio (>1) characteristic of impulsive events.

The four lower panels in Figure 5.7 show the solar wind velocity and the three components of the IMF in the RTN coordinate system. SWEPAM data indicate that during the NR electron event, *ACE* was embedded in a solar wind stream with a mean velocity of 642 km s^{-1}. Both the solar wind velocity and the IMF direction were stable throughout the NR electron event. Therefore, the Parker IMF model and the approximations adopted in the model for particle propagation are reasonable assumptions. The nominal footpoint of the field line connecting *ACE* to the Sun was at W37, as estimated from the observed solar wind speed, which was in between the longitudes of the two western flare sites, W63 and W23. The spectral index of the derived differential intensity spectrum is $\gamma = 2.6$, so we take $\gamma_s = 3.1$ as a first approximation of the spectral index of the electron source (see section 3.6).

5.3.3 Deconvolution of the NR electron event

Figure 5.8 shows the *ACE*/MAG magnetic field measurements in the spacecraft coordinate system, the range of μ-values scanned by the LEFS60 telescope and the μ-co of the telescope

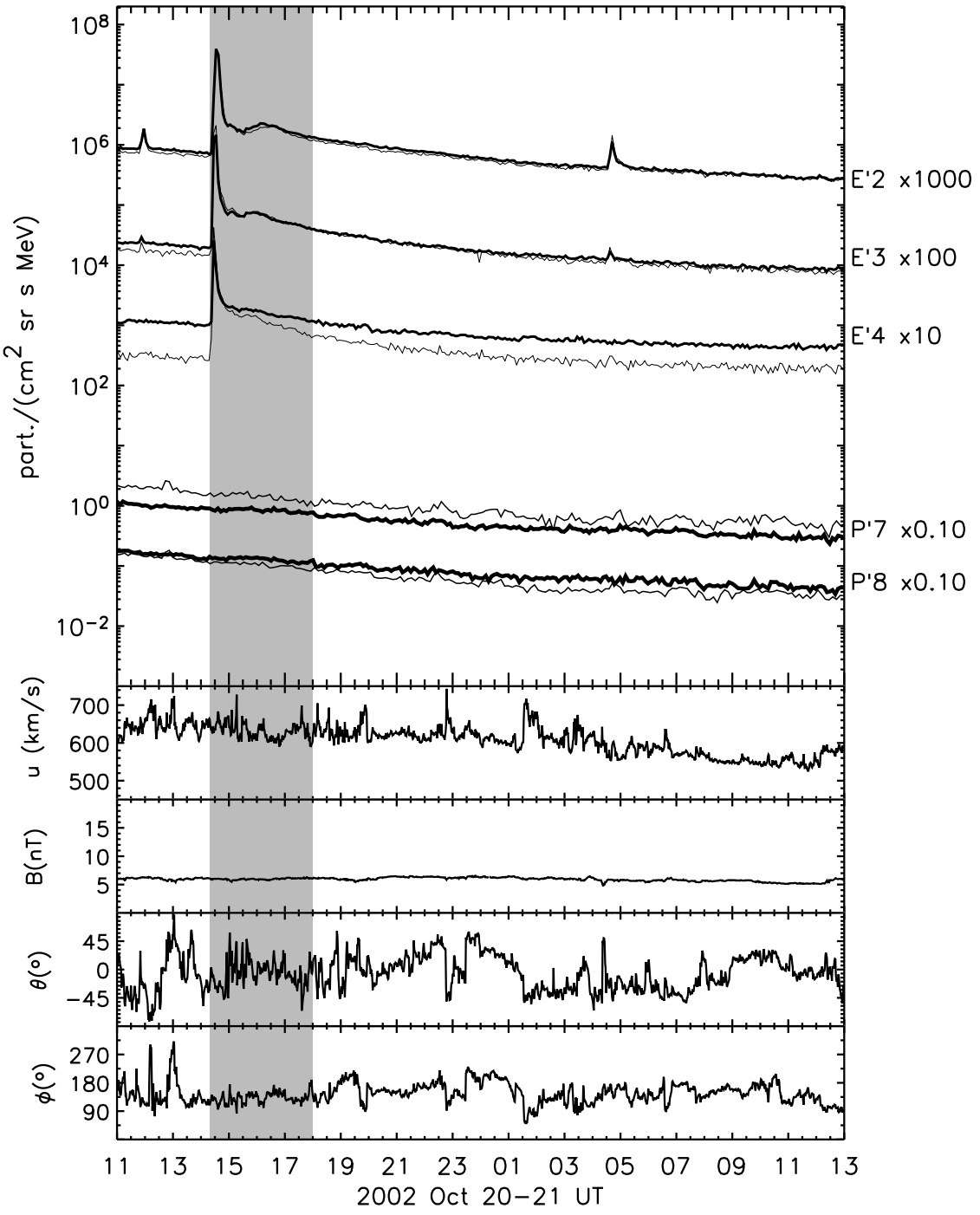

Figure 5.7: Oct02 event: Particle event, solar wind and magnetic field components in the RTN coordinate system. Same presentation as in Figure 5.1.

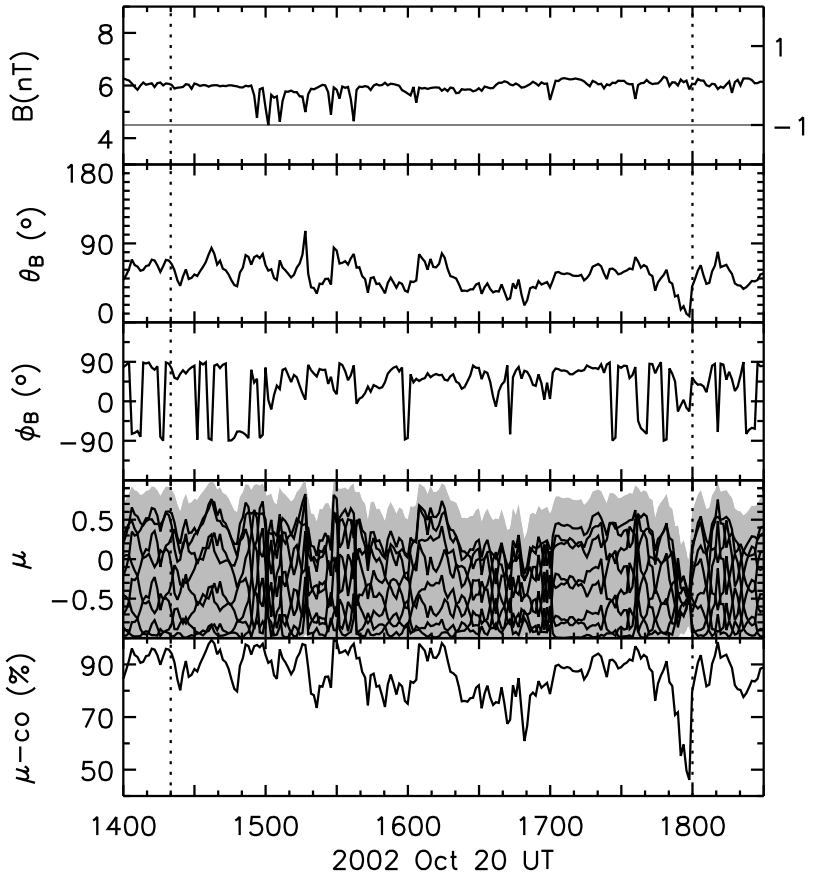

Figure 5.8: Oct02 event: IMF components in the spacecraft coordinate system; μ-range scanned by the LEFS60 telescope (gray area) and pitch-angle cosine of each sector; μ-co. Same presentation as in Figure 5.2.

for the period under study. As can be seen, the IMF polarity remains negative during the period under study; this means that electrons coming from the Sun along the field lines have $\mu = -1$. The μ-co of the telescope varies between 50% and 100%, with a mean coverage, μ-co ∼84%. Since the telescope scans those particles propagating antisunward along the field direction (gray area in panel four) and μ-co $\geq$ 70%, sectored data provides a detailed description of the NR electron event.

We simulate this electron event following the same procedure as described in section 5.2.3 for the May00 event. The lowest values of ζ obtained for each scattering case are listed in Table 5.7. Figure 5.9 shows the fit for the case with the lowest ζ; it corresponds to $\lambda_r = 0.9$ AU and μ-dependent scattering with $\epsilon = 0.01$. The fit succeeds in reproducing most of the profiles for more than three hours. The simulated sectored intensities fit perfectly with observations in sectors 5, 6, 7 and 8; these are the sectors scanning mainly negative μ values. There are, however, discrepancies between the simulated and observed sectored intensities during the 20 min following the peak intensity in the E'2 channel (and partially in E'3) for the sectors

1, 2, 3 and 4. Peak intensities measured by these sectors are about one order of magnitude smaller than the peak intensity of sector 6, for example. The causes of these discrepancies are likely to be the same as the causes for the discrepancies in the May00 event.

The values of the solar electron injection derived from the best fit are shown in the three top panels of Figure 5.10. The total number of injected NR electrons in the whole measurement range is $(5.1 \pm 1.3) \times 10^{33}$, as determined by the normalization of fitting. At low energies (channel E'2) the injection profile clearly shows three components: two prompt components and an extended one. The first prompt component starts around 14:12 UT, lasts ~5 min and it corresponds to the ~92% of the whole injection. A second component (< 1%) can be identified, starting at 14:39 UT and lasting ~1 min. A third weaker (~7%) component starts at 15:28 UT and extends for more than two hours. At low energies (E'2), the first injection component at 14:12 UT shows a previous small component that could be due to secondary responses of the instrument to electrons of higher energy (see discussion in section 5.2.3). Therefore, we assume that the actual first injection component is only the second part of this profile, starting after 14:15 UT in the E'2 energy channel. The three injection components also appear in the E'3 and E'4 energy channels, but with different time cadence and decreasing intensity.

By integrating the injection function over time for each energy channel, we find that the source spectrum can be best fit by a power-law with index $\gamma_s = 3.0$. Thus, there is a good agreement between the spectral index deduced from the time-integrated spectrum and the one estimated from the observations.

The three lower panels in Figure 5.10 compare the timing of the electron injection with the electromagnetic emissions observed at 1 AU, as in Figure 5.5. The first electron injection episode takes place in the ten minutes following the first type III radio emission, in coincidence with the second peak in the soft X-ray flux profile, observed at 14:13 UT and associated with the C6.6 X-ray flare identified in Hα at S13W63 (see Table 5.4). The beginning of the second injection episode seems to be related to: i) the third peak in the soft X-ray flux profile observed at 14:28 UT and associated with the M1.8 X-ray flare (located at S19W23); ii) the hard X-rays burst; iii) the second weak type III burst; and iv) the metric type II burst. Despite the fact that the W23 soft X-ray flare was more intense than the earlier W63 flare, its associated type III burst was weaker and the NR electron injection was much smaller. Therefore, we conclude that the W63 soft X-ray flare was magnetically better connected to the spacecraft than the W23 flare, contrary to the expectation according to the value of the angular distance Δ (see Table 5.4).

The timing of the third injection component is less clear since its beginning is masked by the tail of the second component in the E'4 channel and it seems to start earlier at higher

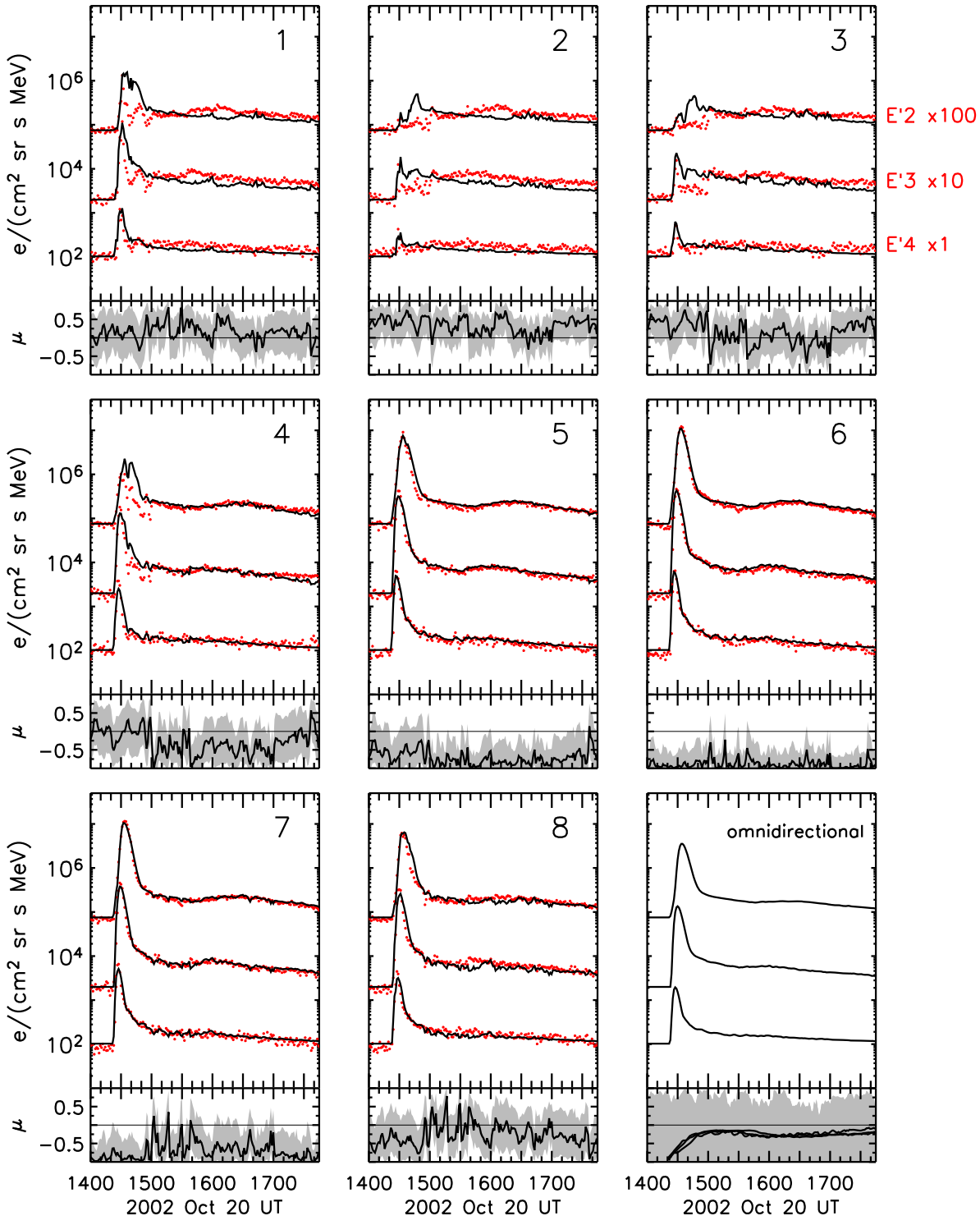

Figure 5.9: Oct02 event: Observational (red dots) and simulated (black line) sectored intensities. Same presentation as in Figure 5.4.

Table 5.7: Results of the fit

Scattering case	ζ {E'2, E'3, E'4}	λ_r (AU)
Isotropic scattering	{38, 39, 16} = 93	0.8
μ-dep with $\epsilon = 0.10$	{33, 32, 14} = 79	0.9
μ-dep with $\epsilon = 0.01$	{32, 29, 16} = 77	0.9

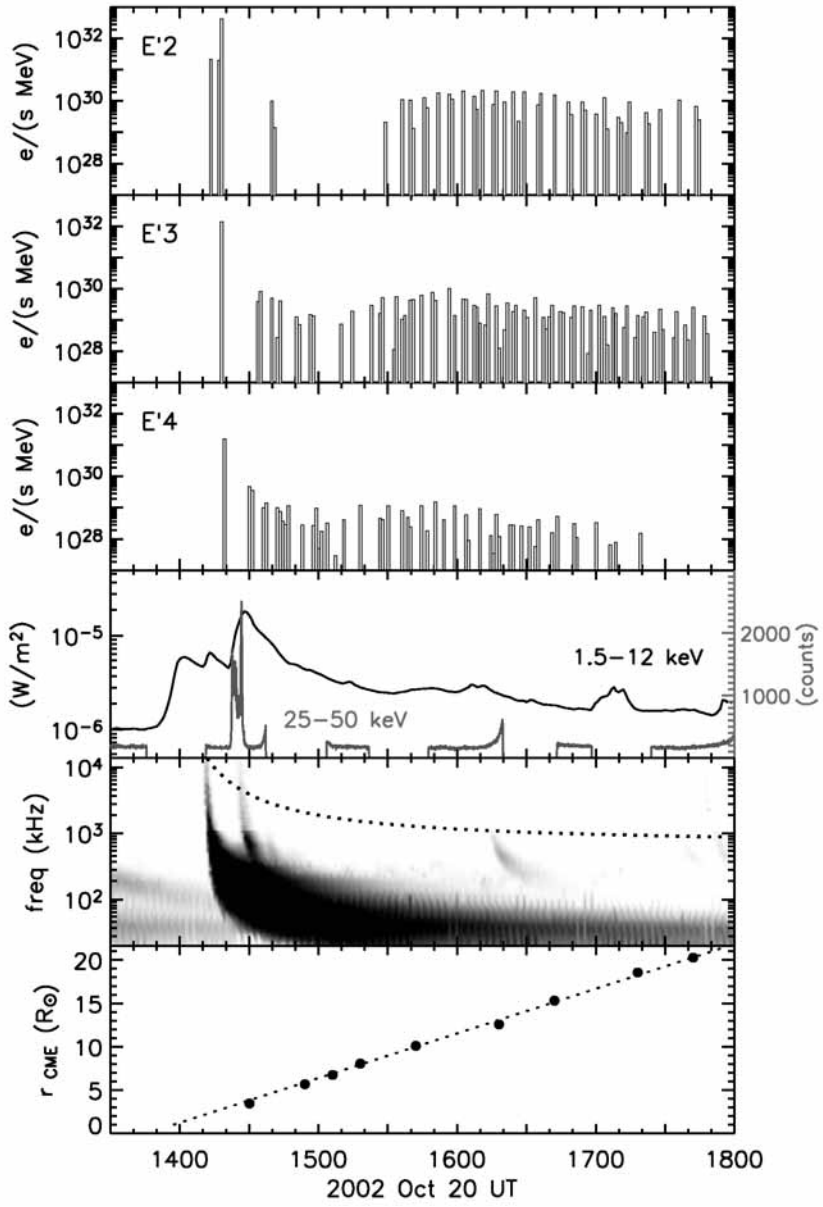

Figure 5.10: Oct02 event: Electron injection and associated electromagnetic emissions. Same presentation as in Figure 5.5.

energies. A faint radio burst observed at ~16:20 UT could be related to a source at a height close to the CME leading edge if the density model of Mann et al. (1999) is assumed (dotted line in the fifth panel of Figure 5.10). Moreover, the CME seems to originate at the same height as the first type III burst. This was already pointed out by Klein & Posner (2005), who found that the source of the first type III burst at 164 MHz projected onto the angular extension of the narrow CME observed by LASCO. Therefore, the timing of the third injection component supports a scenario where the source of the third injection component is related to the CME-driven shock.

We conclude that the NR electron event observed on 2002 October 20 was provided by the flaring activity of the two western active regions, followed by the CME-driven shock originated close to the location of the first western flare.